The Astrophysical Journal, 833:86 (10pp), 2016 December 10 doi:10.3847/1538-4357/833/1/86

ASTROSAT CZT IMAGER OBSERVATIONS OF GRB 151006A: TIMING, SPECTROSCOPY, AND POLARIZATION STUDY

A. R. Rao[1], Vikas Chand[1], M. K. Hingar[1], S. Iyyani[1], Rakesh Khanna[1], A. P. K. Kutty[1], J. P. Malkar[1], D. Paul[1], V. B. Bhalerao[2], D. Bhattacharya[2], G. C. Dewangan[2], Pramod Pawar[2,3], A. M. Vibhute[2], T. Chattopadhyay[4], N. P. S. Mithun[4], S. V. Vadawale[4], N. Vagshette[4], R. Basak[5], P. Pradeep[6], Essy Samuel[6], S. Sreekumar[6], P. Vinod[6], K. H. Navalgund[7], R. Pandiyan[7], K. S. Sarma[7], S. Seetha[7], and K. Subbarao[7]

[1] Department of Astronomy and Astrophysics, Tata Institute of Fundamental Research, Homi Bhabha Road, Mumbai, India; arrao@tifr.res.in
[2] Inter University Center for Astronomy and Astrophysics, Pune, India
[3] S. R. T. M. University, Nanded, India
[4] Physical Research Laboratory, Ahmedabad, India
[5] Nicolaus Copernicus Astronomical Center, Polish Academy of Sciences, Warsaw, Poland
[6] Vikram Sarabhai Space Centre, Thiruvananthapuram, India
[7] ISRO Satellite Centre, Bengaluru, India

Received 2016 July 13; revised 2016 August 23; accepted 2016 September 18; published 2016 December 8

ABSTRACT

AstroSat is a multi-wavelength satellite launched on 2015 September 28. The CZT Imager of *AstroSat* on its very first day of operation detected a long duration gamma-ray burst (GRB), namely GRB 151006A. Using the off-axis imaging and spectral response of the instrument, we demonstrate that the CZT Imager can localize this GRB correctly to about a few degrees, and it can provide, in conjunction with *Swift*, spectral parameters similar to those obtained from *Fermi*/GBM. Hence, the CZT Imager would be a useful addition to the currently operating GRB instruments (*Swift* and *Fermi*). Specifically, we argue that the CZT Imager will be most useful for the short hard GRBs by providing localization for those detected by *Fermi* and spectral information for those detected only by *Swift*. We also provide preliminary results on a new exciting capability of this instrument: the CZT Imager is able to identify Compton scattered events thereby providing polarization information for bright GRBs. GRB 151006A, in spite of being relatively faint, shows hints of a polarization signal at 100–300 keV (though at a low significance level). We point out that the CZT Imager should provide significant time resolved polarization measurements for GRBs that have fluence three times higher than that of GRB 151006A. We estimate that the number of such bright GRBs detectable by the CZT Imager is five to six per year. The CZT Imager can also act as a good hard X-ray monitoring device for possible electromagnetic counterparts of gravitational wave events.

Key words: gamma-ray burst: general – gamma-ray burst: individual (151006A) – instrumentation: detectors – X-rays: general

1. INTRODUCTION

The past decade has seen a tremendous improvement in our understanding of gamma-ray bursts (GRBs), particularly after the launch of *Swift* and *Fermi* satellites (Gehrels 2004; Gehrels & Mészáros 2012).

With its quick localization ability, *Swift* could detect the afterglows of many GRBs and help measure their redshifts (Gehrels et al. 2009). The *Fermi* satellite, on the other hand, provided the widest ever spectral coverage of the prompt emission of GRBs from 8 keV to ∼40 MeV using the GBM instrument, and extending further up to >300 GeV with the LAT instrument for some GRBs (Atwood et al. 2009; Meegan et al. 2009).

A new addition to the suite of instruments studying GRBs is the hard X-ray imager Cadmium Zinc Telluride Imager (CZTI) on *AstroSat*, the Indian multi-wavelength observatory (Singh et al. 2014). CZTI utilizes a coded aperture mask and Cadmium Zinc Telluride detectors (Figure 1, left) to image a $4\overset{\circ}{.}6 \times 4\overset{\circ}{.}6$ area of the sky in the 20–200 keV range (Bhalerao et al. 2016). Apart from this primary coded field of view, CZTI functions as an open detector at energies >100 keV, sensitive to almost the entire sky (Figure 1, right). At these energies, CZTI also has X-ray polarization capabilities (Chattopadhyay et al. 2014; Vadawale et al. 2015). CsI (Tl) scintillators placed below the CZT modules for active anti-coincidence shielding (Figure 1, left) also serve as all-sky high-energy detectors in the 100–500 keV range.

Swift and *Fermi* satellites showcase two different approaches to the study of GRBs. For quick and precise localization, *Swift* uses a Coded Aperture Mask (CAM) and large area pixelated Cadmium Zinc Telluride (CZT) detectors with 4 mm × 4 mm pixels of 2 mm thickness (Barthelmy et al. 2005). At such thickness, CZT detectors have a low spectral response at higher energies (above about 150 keV) and hence BAT by itself cannot precisely measure the peak energy of hard GRBs. In fact the number of short GRBs detected by *Swift* is much lower than that detected by other instruments, particularly due to the lack of response to high-energy X-rays (Band 2006). On the other hand, *Fermi* uses multiple open NaI crystal detectors (Meegan et al. 2009) and localizes the GRBs by comparing the relative counts in the different detectors. Hence the resultant localization accuracy is poor (several degrees) and the energy resolution of the detectors is rather modest (Meegan et al. 2009). Consequently, the prompt spectral studies are hampered, and hence a good understanding of the radiation mechanism during the prompt phase is lacking. With its wide field of view, high-energy coverage, and good spectral resolution, CZTI thus fills the gap between the capabilities of *Swift* and *Fermi*.

On the very first day of operation, CZTI detected GRB 151006A (Bhalerao et al. 2015). GRB 151006A was

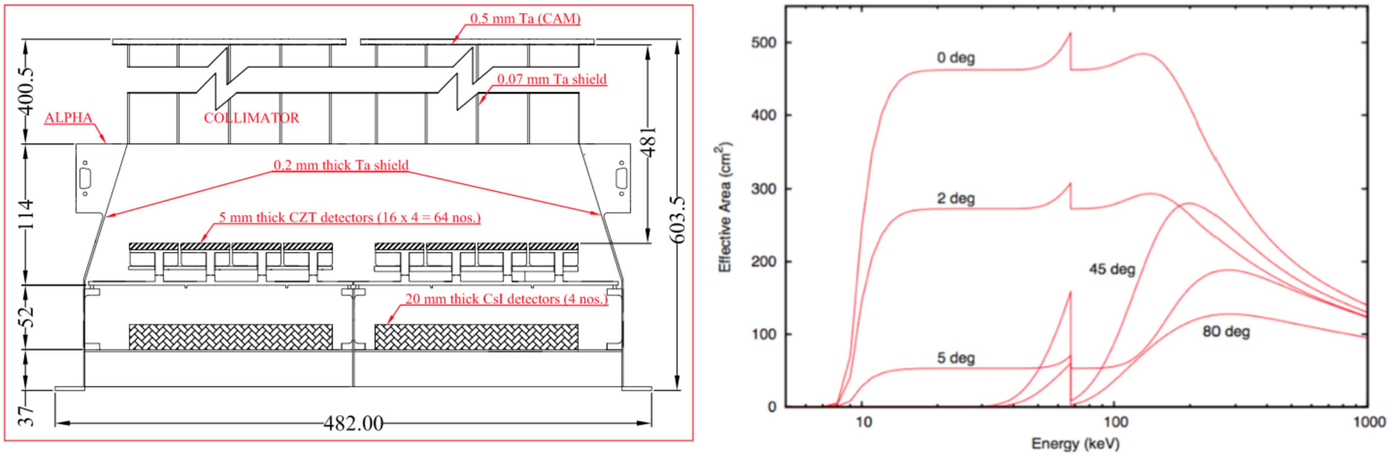

Figure 1. Left: a schematic diagram of the CZT Imager instrument on board the *AstroSat* satellite. All dimensions are in millimeters. A Tantalum coded aperture mask (CAM) at the top is backed by 400 mm Al/Ta collimators, which restrict the field of view to $4\overset{\circ}{.}6 \times 4\overset{\circ}{.}6$. Four identical quadrants with 4×4 arrays of 5 mm thick CZT modules forms the focal plane, 481 mm below the CAM. The 2.46 mm pixels matched to the CAM pitch provide a native angular resolution of $\sim 17'$ in the primary field of view. 20 mm thick CsI(Tl) scintillators mounted $\sim$66 mm below the CZT modules provide active anti-coincidence shielding, and also function as a wide-angle detector in the 100–500 keV range. Right: effective area of CZT Imager as a function of energy. The different lines are for sources at different angles from the CZTI viewing axis (marked in the figure). The sharp rise at $\sim$57 keV is due to the K-edge of Ta.

first reported by *Swift*-BAT (Kocevski et al. 2015) at $\alpha = 09^{h}49^{m}48^{s}$, $\delta = +70°30'31''$. The prompt emission lasted for more than 300 s and, subsequently, detection by other X-ray and Gamma-ray missions were reported in a series of GCN circulars. *Fermi* triggered $\sim$4 s before *BAT* and reported a T_{90} of $\sim$84 s (Roberts & Meegan 2015). Due to the wide angle detection capabilities of CZTI, GRB 151006A was registered in CZTI even though the incident angle was as large as $\sim 60°$ from its pointing direction (Bhalerao et al. 2015). The presence of double Compton events is also seen in CZTI, which will help measure the polarization of the GRB (Vadawale et al. 2015). Coincidentally, GRB 151006A is also the first detected GRB in the CALorimetric Electron Telescope (CALET) on board the International Space Station Gamma-Ray Burst Monitor detection (CGBM). CGBM reported a double peak separated by 4 s (Yoshida et al. 2015).

In this paper, we present the results of the CZTI observations of GRB 151006A. We demonstrate that CZTI with *Swift* can give spectral parameters similar to that obtained by *Fermi*/GBM and CZTI can localize this GRB correct to a few degrees. We also present some results of the measurements of hard X-ray polarization in this GRB and show that CZTI will be very useful in constraining the emission mechanism in the prompt phase of GRBs. A detailed description of the CZT Imager is given in Bhalerao et al. (2016) and details of on board performance and spectral fitting methodology are given in Vadawale et al. (2016) and Chattopadhyay et al. (2016). For the sake of completeness, however, some salient technical details of the CZT Imager are given in the following sections while discussing results like light curves, spectra, localization, and polarization.

2. OBSERVATIONS AND DATA REDUCTION

2.1. *Swift-BAT*

The *Swift*-BAT data were retrieved from HEASARC's data outlet.[8] Light curves with 1 s time bins in different energy ranges were made by making use of `HEASOFT-6.17`, `FTOOLS`, and the recipe as described in the *Swift*-BAT software guide.[9] We applied gain correction using `bateconvert`, then `batbinevt` was utilized to produce light curves after making a detector plane image (dpi), retrieving problematic detectors, removing hot pixels and subtracting the background using `batbinevt` again, `batdetmask`, `bathotpix`, and `batmaskwtevt`, respectively. The background subtraction is an advantage with coded aperture masked detectors.

The time integrated *Swift*-BAT spectrum is obtained in the BAT mission elapsed times (METs) corresponding to the times of our selection for joint time-integrated spectral analysis (465818107.555—465818198.115 BAT MET). The steps followed to obtain the BAT spectrum are the same as those described above to obtain BAT light curves and additional `FTOOLS` `batupdatephakw` and `batphasyserr` are used for compensating the observed residual in the responses and for making sure that we have the position of the burst in instrument coordinates. We have generated the detector response matrix (DRM) using `batdrmgen`.

2.2. *Fermi*

Fermi-GBM has 12 thallium activated sodium iodide (NaI) detectors and 2 Bismuth Germanate (BGO) detectors, covering energy ranges of 8.0 keV–1000 keV and 200 keV–40 MeV respectively (Meegan et al. 2009). The NaI 0, 1, 3 (hereafter referred to as $n\#$, where $\#$ is the detector number) registered higher fluence than the other NaI detectors as seen in the quick look data from the *Fermi* GRB burst catalog on HEASARC.[10] Time tagged event data are available for the complete range spanning the T_{90} of this GRB and we make use of this data for both timing and spectral analysis. We used BGO 0 for timing and spectral analysis of the GRB. We choose n0 for making

[8] HEASARC archive: https://heasarc.gsfc.nasa.gov/cgi-bin/W3Browse/w3browse.pl.

[9] *Swift*-BAT guide: http://swift.gsfc.nasa.gov/analysis/bat_swguide_v6_3.pdf.

[10] *Fermi* GRB catalog: https://heasarc.gsfc.nasa.gov/W3Browse/fermi/fermigbrst.html.

GBM/NaI light curves. The background was fitted in the time intervals −100 s to −10 s and 100 s to 300 s w.r.t. GBM trigger time[11] using GBM software rmfit 4.3.2.[12] The light curves were re-binned to 1 s and obtained in the energy bounds 8–25 keV, 25–50 keV, 50–100 keV, and 100–200 keV for n0. For BGO 0, we made a light curve in the 200–500 keV region using again the same tool as n0.

For spectral analysis with *Fermi*, we chose the brightest three NaI n0, n1, and n3 and BGO 0 as before. We used *rmfit* software to extract the time integrated spectrum from the time tagged event (TTE) files. The background spectrum was extracted in the time intervals that are specified earlier. For the time integrated spectral analysis of this GRB, we choose an interval of −5.5 s to 85.2 s with respect to the GBM trigger time. The spectral response for each detector is provided by the instrument team as an RSP2 file that contains responses for each 2 degree change in the pointing of the *Fermi* spacecraft. Our selected time interval was spread over two extensions; therefore, we generated a weighted response using gtburst[13] tool of the Fermi science tools.

2.3. CZTI

Data from CZTI consist of individual time-tagged photon information for the X-rays registered in the CZT detectors. This information contains identification of the position of interaction (pixel ID), the energy of the event, the time of registration of the event correct to 20 μs, information regarding whether there is a simultaneous event from the alpha tagged detector, and information regarding whether there is a simultaneous event in the Veto detector and the energy of the veto event (Bhalerao et al. 2016). The absolute timing has been verified to be better than 200 μs, while energy information is accurate to 0.5 keV. Data from each quadrant are available separately and independently.

The veto detector provides spectra and light curves at a 1 s time resolution. The channel to energy conversion in the Veto detector is done based on the ground calibration and it is estimated that the combined effect of temperature variation, positional dependence, etc., can lead to an energy uncertainty of 20% in the energy range of 50–500 keV.

CZTI data and Veto detector data were reduced using standard FTOOLS-compatible pipelines[14] to extract spectra and light curves.

GRB 151006A occurred at an angle of 60°.7 from the nominal pointing direction of CZTI, far outside the primary field of view (Figure 4). The coded aperture mask is completely ineffective for localizing such sources, and we cannot use the nominal effective area or response files for analysis. The inhomogeneous mass distribution around the CZT detector modules (instrument housing, collimators, etc.; see Figure 1) results in an energy-dependent transmittivity for every line of sight. Even for a given direction, this transmittivity is different for each CZT pixel.

We have developed a ray-tracing code to estimate the effective area of each pixel in the detector plane for an object at a given location in the sky. The mechanical structure given in Figure 1 is represented by 63 distinct surfaces, which are converted into as many cuboids defined by area, thickness, absorbing material, and orientation with respect to the detector surface. For each pixel, the efficiency of transmission through all of this material is calculated, along with the detection efficiency of the detectors and geometric projection terms, to give an effective area for a given source direction and energy. The blocking parts of the satellite along these lines of sight have been assumed to be low-*Z* materials, and have been ignored in this simulation.

For spectral analysis of GRB 151006A, we used the *Swift*-BAT position to generate effective areas and responses independently for CZT and the Veto detectors, separately for each quadrant for the latter. A Gaussian response is generated for CZT with channels numbered from 1 to 512 and Full Width at half maximum (FWHM) of 2.5 keV. Quadrant wise responses were generated for the Veto detector with channels ranging from 0 to 255 and FWHM of 13.04 keV.

3. RESULTS

3.1. Light Curves

The combined light curves of GRB 151006A using data from *Fermi*, *Swift*, and CZTI are shown in Figure 2. The panels are arranged with increasing energy from top to bottom, and data from different detectors are shown in the same panels for similar energy ranges. The observed count rates in BAT, normally given as count s^{-1} per detector element, are multiplied by 1000 so that they roughly scale to the total observed counts. The vertical dashed lines indicate the time range chosen for spectral analysis (Section 3.2). Error bars are not shown; however, the typical errors in CZTI data are indicated in the figure with comparative numbers from *Fermi*.

We fit the light curves with the Norris model (Norris et al. 2005), which describes the temporal profile of GRB pulses with the following equation:

$$I(t) = A\lambda \exp[-\tau_1/(t - t_i) - (t - t_i)/\tau_2], \qquad (1)$$

Here, t is time since trigger, t_i is the pulse start time, τ_1 and τ_2 are the scaling times of the pulse rise and pulse decay, A is the pulse amplitude, and the constant $\lambda \equiv \exp[2(\tau_1/\tau_2)^{1/2}]$. The pulse width, w, is derived from the rise and decay time of the pulse as $\tau_2(1 + 4\sqrt{\tau_1/\tau_2})^{0.5}$, and the asymmetry of the pulse is τ_2/w. The pulse shape parameters for different energy bands are given in Table 1 for *Fermi* and CZTI data. It can be seen that the parameters derived from the CZT and Veto detectors agree with that of the BAT and GBM pulses. Note that the pulse start time t_i is poorly constrained and when we fix this value for CZTI data to that obtained from GBM, we get comparable values of χ^2. Furthermore, the measured peak count rates have comparable signal-to-noise ratios in CZTI and *Fermi* demonstrating that above 100 keV CZTI is as sensitive as *Fermi* for detecting GRBs.

3.2. Spectral Analysis

Many physical and empirical models have been used for GRB spectral analysis, for instance, the Band function (Band et al. 1993; Goldstein et al. 2013; Gruber et al. 2014), Band + blackbody (Guiriec et al. 2011; Axelsson et al. 2012; Burgess et al. 2014), blackbody with a power law (Ryde 2005; Ryde &

[11] Throughout this paper, time is referred everywhere with reference to *Fermi*-GBM trigger time, unless otherwise mentioned.
[12] http://fermi.gsfc.nasa.gov/ssc/data/analysis/rmfit/.
[13] *Fermi* gburst tool: http://fermi.gsfc.nasa.gov/ssc/data/analysis/scitools/gtburst.html.
[14] CZTI processing pipeline and CALDB files are available under the "Data and Analysis" section of the Astrosat Science Support Cell, http://astrosat-ssc.iucaa.in.

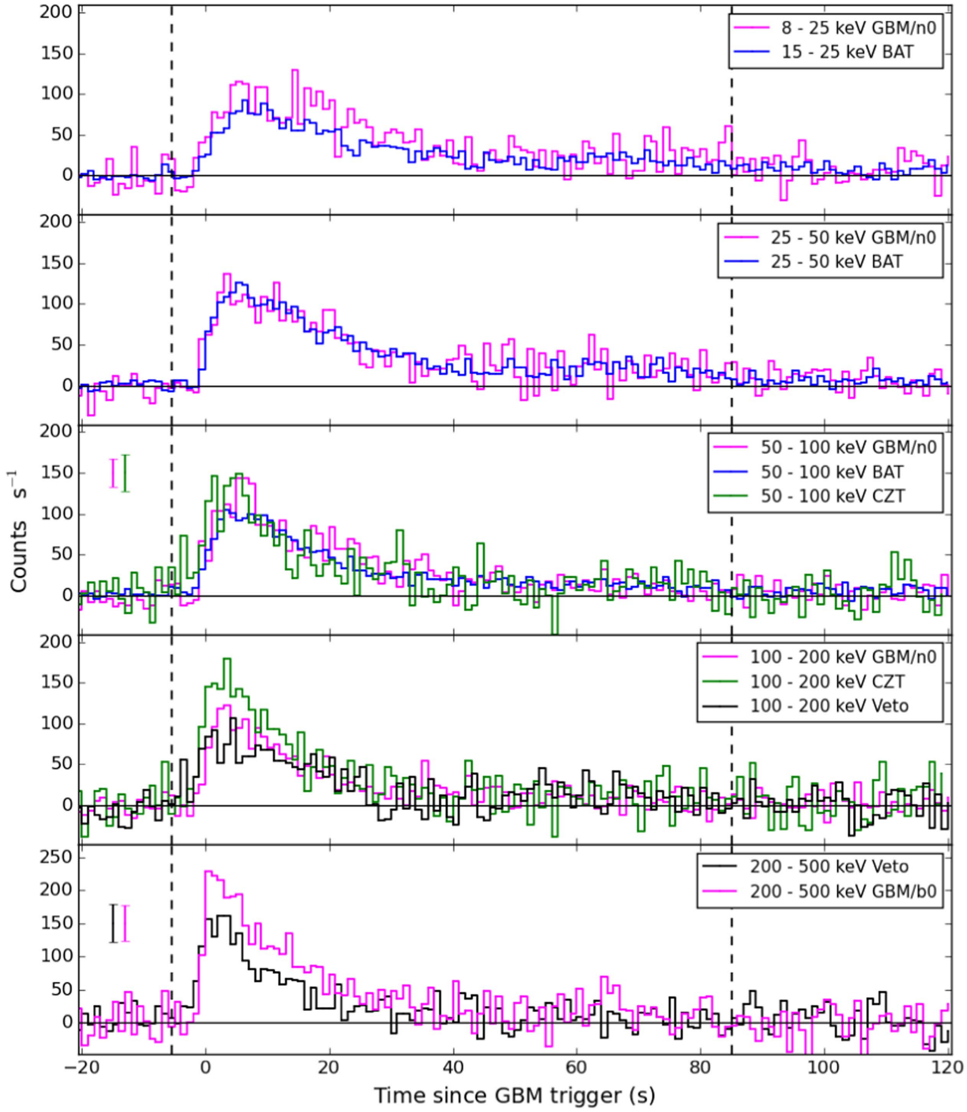

Figure 2. Light curves of GRB 151006A using GBM, BAT, and CZTI data in denoted energy bands. Time is w.r.t. GBM trigger time and the bin size is 1 s. BAT light curves shown here are in counts/s/illuminated detector and are scaled 1000 times to plot along with GBM light curves. The vertical black dashed lines show the time range used for time integrated spectral analysis. Error bars are not shown, but the typical error bar of CZTI, along with that from GBM, is shown in the third and fifth panels from the top.

Pe'er 2009; Page et al. 2011; Sparre & Starling 2012), double blackbodies with a power law (Basak & Rao 2015; Iyyani et al. 2015), etc. Here we examine the time integrated spectrum of GRB 151006A with a few of the above mentioned models, primarily to emphasize the ability of the joint spectral analysis of BAT and CZTI data to produce spectral fit results consistent with those of *Fermi* GBM. We make our spectral analysis using four sets of data: (a) GBM, (b) GBM jointly with CZTI, (c) BAT, and d) BAT jointly with CZTI.

To start with, we use the Band model to fit all four sets of data. The best-fit parameters are given in Table 2, the data and the results are given in Table 2, and the unfolded spectra along with the residuals, given in terms of χ, that is (data-model) scaled to the error in the data, are shown in Figure 3, for all four sets of data. It can be seen that the high-energy index, β is not constrained using only the BAT data (due to the limited high-energy response), but are constrained in all of the other data sets. The obtained values of β being greater than -2 indicates the presence of high-energy emission beyond the currently analyzed energy window of the detectors. An examination of the residuals shows that CZTI data are consistent with the others, though the use of CZTI data gives a slightly higher value of reduced χ^2. We also find that the cross-normalization values for CZTI are within 20% of other detectors. For example, for the BAT data jointly fit with CZTI data, the BAT normalization with respect to the CZT detector is 0.8 ± 0.1, whereas the normalization of Veto detectors agrees with CZT detectors within errors. For GBM jointly fit with CZTI data, the CZT detector normalization with respect to GBM n0 is 0.8 ± 0.1.

The fit values of the parameters obtained for other models (BBPL and 2BBPL), along with the parameters for the Band model, are listed in Table 3 for BAT jointly with CZTI and GBM data to show the effectiveness of using CZTI data with BAT to extend the energy bandwidth. The models have comparable reduced χ^2s. The CZTI spectral data have scattered and fluorescent components in the $<$100 keV region, and hence data above 100 keV, are considered for spectral fitting. For the

Table 1
A Fit to the Pulse Profile of GRB 151006A in Tabulated Energy Bands with the Norris Model (Section 3.1)

Detector	t_i (s)	$\tau1$ (s)	$\tau2$ (s)	Norm counts s^{-1}	χ^2_{red}	w (s)	κ
			50–100 keV, E_{mean} = 75 keV				
Fermi GBM n0	0.1 ± 1.8	0.30 ± 0.67	21.0 ± 2.1	116 ± 10	1.07	26 ± 14	0.82 ± 0.52
CZTI	−1.4 ± 0.6	0.03 ± 0.32	17.5 ± 2.6	93 ± 25	0.8	19 ± 43	0.92 ± 2.2
			100–200 keV, E_{mean} = 150 keV				
Fermi GBM n0	−1.43 ± 0.26	0.84 ± 0.20	15.3 ± 1.2	102.2 ± 5.2	0.99	21.2 ± 2.3	0.72 ± 0.13
CZTI	−1.43[a]	0.03 ± 0.02	15.1 ± 1.4	126.4 ± 6.5	0.83	16.3 ± 3.9	0.92 ± 0.31
	−4.0 ± 0.44	1.29 ± 0.76	13.3 ± 1.5	113.3 ± 6.5	0.70	19.9 ± 3.9	0.67 ± 0.20
Veto	−1.43[a]	0.18 ± 0.14	18.0 ± 2.5	85.8 ± 6.0	0.58	21.3 ± 5.9	0.84 ± 0.35
	−2.8 ± 0.9	1.00 ± 1.15	16.2 ± 2.9	81.7 ± 7.3	0.57	22.9 ± 8	0.7 ± 0.38
			200–500 keV, E_{mean} = 350 keV				
Fermi GBM b0	−1.0 ± 0.2	0.00 ± 0.17	15.6 ± 1.5	245 ± 929	1.1	15.61	1
Veto	−1.14 ± 0.6	0.06 ± 0.28	12.8 ± 1.6	158 ± 25	0.52	15 ± 15	0.88 ± 1.04

Note.
[a] Parameter held fixed in fit.

Table 2
Band Model Fit Parameters for *GRB*151006*A*

Parameter	GBM	GBM+CZTI	BAT	BAT+CZTI
α	$-1.1^{+0.2}_{-0.1}$	$-1.08^{+0.19}_{-0.13}$	$-1.2^{+0.4}_{-0.1}$	$-1.22^{+0.29}_{-0.18}$
β	$-1.8^{+0.1}_{-0.1}$	$-1.75^{+0.1}_{-0.1}$	$-1.71^{+0.19}_{-10}$	$-1.8^{+0.26}_{-0.4}$
E_p (keV)	218^{+126}_{-78}	$189.0^{+87.2}_{-66.5}$	159^{+536}_{-82}	$160.26^{+214.84}_{-67.0}$
Norm[a]	$5.0^{+2.0}_{-1.0}$	$5.3^{2.27}_{-1.0}$	$3.6^{+3.9}_{-1.2}$	$4.31^{3.10}_{-1.56}$
χ^2_{red}	0.67	1.10	0.81	1.53

Note.
[a] Norm is in units of 10^{-3} photons cm^{-2} s^{-1} keV^{-1}.

spectral fit with the 2BBPL model, however, the CZTI + BAT data shows a peak at 1 MeV. On careful inspection, the time resolved data showed the presence of multiple thermal components (up to three black bodies) and the time integrated spectra favored some of these components depending on the bandwidth of the instruments. A detailed time resolved spectral investigation, including *Fermi*-LAT data, would be reported elsewhere.

3.3. Localization

We explore the possibility of using this information to localize transient events like GRB 151006A, occurring outside the FoV of CZTI. Spectra were obtained covering the time duration shown in Figure 2 and the background spectra were obtained by adding pre-burst and post-burst intervals of durations of 90 s and 200 s respectively.

We have used the spectral form obtained from the Band model fit and calculated the pixel wise efficiency for energies in steps of 5 keV. The estimated counts for each of the 64 CZT detector modules, for the *Swift* position of this GRB (see Figure 4) are shown in Figure 5 (top panel) as a continuous line. Overplotted on this figure are the observed counts. A reasonable agreement between the two are seen.

To test the localization capabilities of the CZTI, we simulated the instrument response in a grid of θ_x, θ_y coordinates (see Figure 4) using the spectrum and fluence of GRB 151006A. We then binned the counts by detector, and compared these simulations with the observed values. The χ^2 as a function of local θ_x, θ_y coordinates is shown in Figure 5 (middle panel). The actual position of the GRB is marked with a cross. We can see that CZTI could have localized this GRB with an uncertainty of about 10°. In order to estimate the contribution of Poisson error to the data, we repeated the exercise by comparing simulated detector-wise counts for GRB 151006A from the θ_x, θ_y grid with simulated counts for the true location, and calculating the χ^2 for each direction (Figure 5, bottom panel). It is seen that CZTI can localize bright GRBs with an accuracy of a few degrees. The difference between this idealized case and real data may arise from three primary effects: (a) non-Poissonian errors in the data due to Cosmic Ray interactions, (b) effects of scattering in the detector material, and (c) effects of un-modeled absorption in other parts of the spacecraft. A full mass model of the satellite is being prepared and a GEANT-4 simulation for the response of an off-axis GRB is being carried out to understand these systematics. The results of this exercise will be reported elsewhere.

3.4. Polarization

The prompt emission from a GRB is expected to be highly polarized owing to the non-thermal origin of the radiation. This is corroborated by the recent findings of high degrees of polarization in the prompt emission of a few GRBs by *RHESSI*, *INTEGRAL*, and GAP (Coburn & Boggs 2003; McGlynn et al. 2007, 2009; Götz et al. 2009, 2013; Yonetoku et al. 2011, 2012). The reported degrees of polarization in the X-ray/gamma-ray band of the prompt emission are in most cases quite high (60%–80%; see the review by Covino & Gotz 2016) and these are explained in the standard fireball model of GRBs (Meszaros & Rees 1993) as being due to synchrotron emission with a uniform magnetic field either carried by the outflow (Nakar et al. 2003) or locally produced at the shock (Medvedev 2007). An even higher degree of polarization can be produced if the primary radiation mechanism is Compton Drag, i.e., inverse Compton emission from relativistically outflowing electrons in the jet (Lazzati et al. 2004). A similar mechanism operates in the cannonball model (Dado et al. 2007), which advocates bulk Comptonization as the primary source of

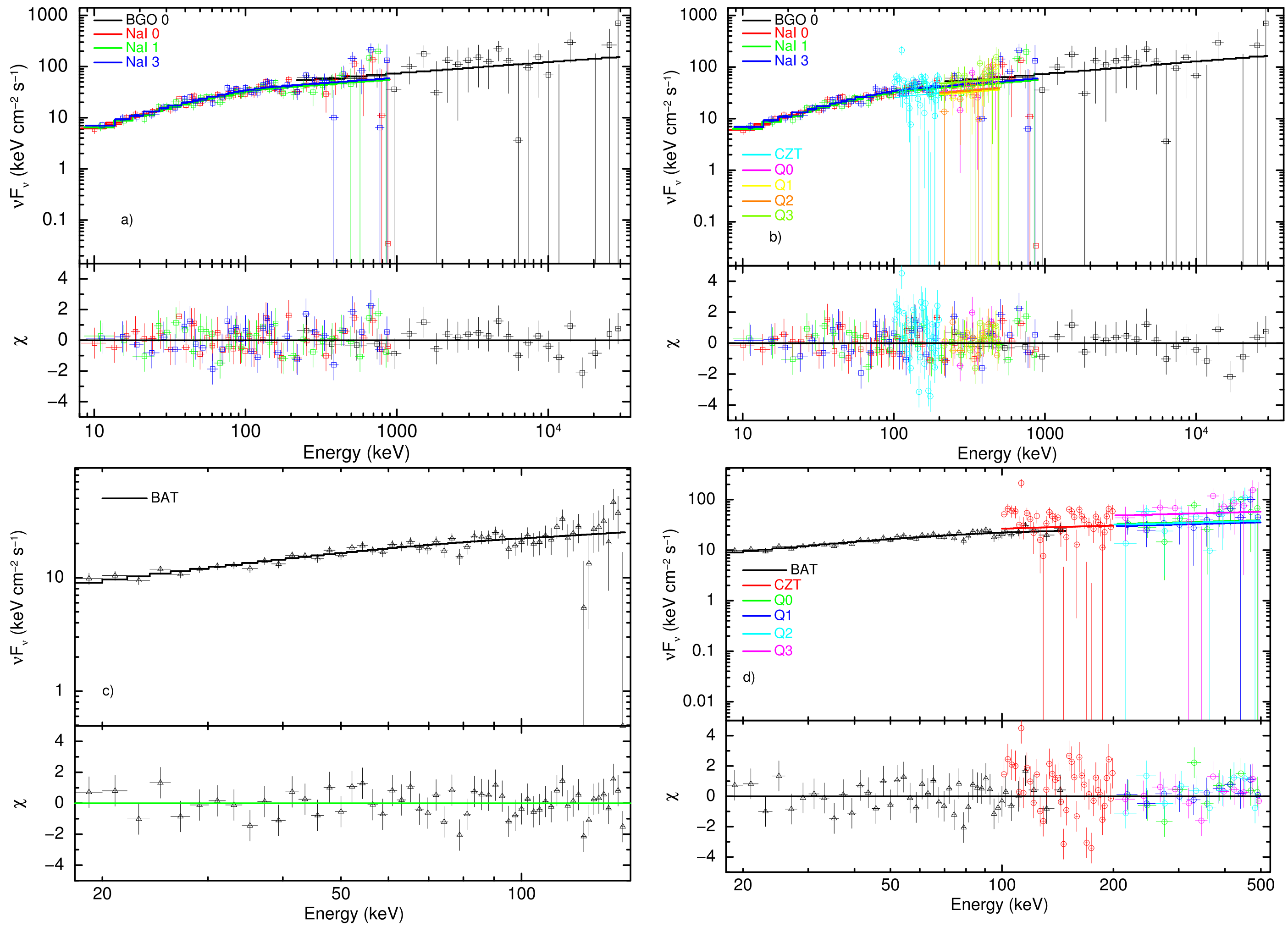

Figure 3. Unfolded energy spectrum of GRB 151006A and the residuals (given in terms of χ, that is (data-model) scaled to the error in the data) are shown based on the spectral fits for the Band model in the time interval −5.5 s to 85.2 s, for the data obtained from (a) *Fermi* GBM, (b) CZTI combined with *Fermi* GBM, (c) *Swift*-BAT, and (d) CZTI combined with *Swift*-BAT.

GRB prompt emission. On the other hand, evidence of thermal photospheric emission has been reported in many cases of prompt GRB emission (Pe'er & Ryde 2016). This component, while potentially providing seed photons for Compton drag, would contribute little to polarized emission by itself and hence reduce the overall degree of polarization.

CZTI can help the study of GRB polarization by measuring X-ray polarization in the 100–300 keV range. In this energy range, CZTI collimators and support structure are highly transparent. Most of the photons with these energies undergo Compton scattering in pixels of CZTI, and the secondary photon is photo-absorbed in a nearby pixel. The direction of scattering depends on the degree and direction of polarization of the source, and this effect can be exploited to measure source polarization (Chattopadhyay et al. 2014; Vadawale et al. 2015). An additional advantage of CZTI polarimetry is that the polarization information can be obtained from the available raw data in standard mode itself without any requirement of changing the hardware configuration.

The photons are expected to be preferentially scattered in the direction perpendicular to the polarization direction, giving rise to an asymmetry/modulation in an otherwise flat azimuthal angle distribution. Amplitude of the modulation is directly proportional to the polarization fraction embedded in the incident radiation. True Compton events can be separated from chance two-pixel events by applying three criteria: (1) spatial proximity of pixels, (2) temporal coincidence: events must be recorded within 40 μs of each other,[15] and (3) the sum and ratio of deposited energies must be consistent with those expected from true Compton events. Selection procedure of the Compton events in CZTI has been discussed in detail in Chattopadhyay et al. (2014).

Figure 6 shows the one second light curve (with an arbitrary time reference) in Compton events (in black points) for the orbit in which the GRB 151006A was detected. Clear detection of the GRB in the Compton events demonstrates the pertinence of the selected Compton events. Furthermore, if we do not apply the Compton criteria (which means selecting only the non-neighboring pixels without putting any Compton energy criteria), the GRB does not show up in the light curve as shown by the red data points. This gives additional confidence in the selection of Compton events from the raw event mode data.

The Compton events in the time window of 34 s from the onset of the GRB prompt emission (under the shaded region in Figure 6) are analyzed further to obtain their azimuthal angle

[15] CZTI has a time resolution of 20 μs and we use two clock ticks as the proximity window.

Table 3
Swift/-*BAT* + *AstroSat*/*CZTI* and *Fermi*/*GBM* Fit Parameters for GRB151006A

Instrument	Parameters	Band	BBPL	2BBPL
BAT + CZTI	α/Γ	$-1.22^{+0.29}_{-0.18}$	$1.64^{+0.17}_{-0.15}$	$1.75^{+0.37}_{-0.19}$
	$E_{\rm norm}$ (keV)/$\Gamma_{\rm norm}$[a]	100.0	$4.0^{+3.7}_{-1.9}$	$6.00453^{+15.4}_{-3.2}$
	E_p/kT_1 (keV)	$160.26^{+214.84}_{-67.0}$	$22.1^{+4.4}_{-5.4}$	$23.2^{+3.6}_{-4.3}$
	$BB_{\rm norm}$[a]	…	$0.22^{+0.19}_{-0.14}$	$0.31^{+0.24}_{-0.18}$
	β/kT_2	$-1.8^{+0.26}_{-0.4}$	…	$1098^{+\infty}_{-574}$
	$\mathrm{Band}_{\rm norm}$ $10^{-3}/BB_{\rm norm}$[a]	$4.31^{3.10}_{-1.56}$	…	$76.7^{173.4}_{-86.4}$
	$\chi^2_{\rm red}$	1.53	1.52	1.52
GBM	α/Γ	$-1.1^{+0.2}_{-0.1}$	$1.53^{+0.06}_{-0.05}$	$1.5^{+0.1}_{-0.1}$
	$E_{\rm norm}$ (keV)/$\Gamma_{\rm norm}$[a]	100.0	$2.6^{+0.6}_{-0.5}$	$2.2^{+1.3}_{-0.7}$
	E_p/kT_1 (keV)	218^{+126}_{-78}	$30.0^{+7.4}_{-6.3}$	$46^{+615.4}_{-13}$
	$BB_{\rm norm}$[a]	…	$0.3^{+0.1}_{-0.1}$	$0.5^{+0.2}_{-0.3}$
	β/kT_2 (keV)	$-1.8^{+0.1}_{-0.2}$	…	$12.6^{+\infty}_{-3.7}$
	$\mathrm{Band}_{\rm norm}$ $10^{-3}/BB_{\rm norm}$[a]	5^{+2}_{-1}	…	$0.15^{+0.3}_{-0.1}$
	$\chi^2_{\rm red}$	0.67	0.7	0.69

Note.
[a] photons $\mathrm{cm^{-2}\ s^{-1}\ keV^{-1}}$.

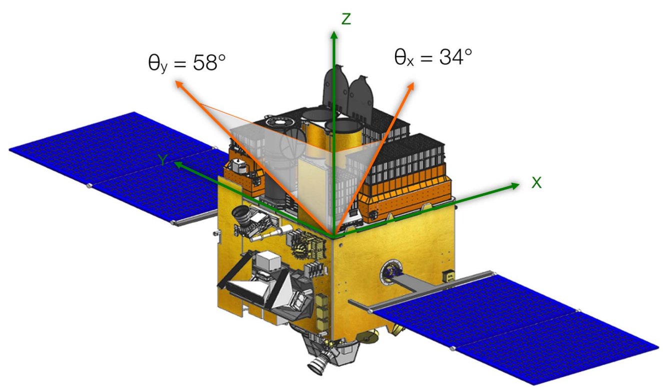

Figure 4. Schematic picture of *AstroSat* showing the local coordinate definition with respect to the CZT Imager instrument. Localization is calculated in units of θ_x (θ_y), angles measured from the Z axis in the ZX (ZY) planes. The two components of the incident direction of GRB 151006A in this coordinate system are indicated.

distribution. Figure 7 (top) shows the raw eight bin azimuthal angle distribution for these events (shown in black) after subtracting the background azimuthal distribution from that of the events in the shaded region in Figure 6, which contain contributions from both GRB prompt emission and the background. The background azimuthal distribution is computed from the existing pre- and post-GRB events. The red bars stand for the simulated azimuthal angle distribution for a 100% unpolarized beam of spectrum and angle of incidence the same as the GRB. It is to be noted that the Geant-4 simulation for the unpolarized radiation is done with a zeroth order of the CZTI mass model. Detailed Geant-4 simulation with the complete mass model of CZTI along with the satellite structure and other instruments is currently in progress. The significant deviation in the azimuthal angle distribution of the observed events from that of the events from an unpolarized beam hints at the presence of a polarization signature in the prompt emission of GRB 151006A; though, the statistical significance is low due to the small number of valid Compton events registered from the GRB. The raw azimuthal distribution is then corrected for the geometry of the CZTI pixels as well as for the off axis response by normalizing the GRB azimuthal distribution with respect to the simulated unpolarized distribution. The result is shown in Figure 7 (bottom). The red solid line in this figure is a $\cos^2\phi$ fit to the modulation pattern. The fitted modulation factor μ is quite high and it has a value of ~0.32 with a detection significance of 1.5σ. Such a high modulation factor would imply that the GRB prompt emission is highly polarized. However, precise polarization measurement requires the detailed mass model of CZTI along with the satellite and other instruments. While this is currently being pursued, the result presented above is a tantalizing hint of a polarization signature in GRB 151006A.

It is to be noted that the Crab Nebula has been observed by CZTI for more than 500 ks and a preliminary analysis shows the presence of a statistically significant polarization signature in the Crab (S. V. Vadawale 2016, in preparation). One of the advantages of GRB polarimetry with CZTI compared to Crab or any other bright persistent X-ray source is the availability of background events immediately before and after the GRB, which is extremely important to quantify the source azimuthal angle distribution. This makes GRB polarimetry with CZTI even more promising.

Although in the case of GRB 151006A, the statistical significance of the obtained modulation is low, the detection of the GRB in the Compton events and thereafter finding a distinct modulation pattern in the azimuthal angle distribution from these Compton events clearly implies that CZTI does have a significant polarization measurement capability for off-axis GRBs, even for those with moderate brightness, such as GRB 151006A.

It is to be noted that this is the first time that the polarization signature in a GRB of such a moderate brightness has been reported. Other GRBs for which polarization measurements have been reported so far are at least 5–10 times brighter than GRB 151006A. Therefore, brighter GRBs detected by the CZTI would certainly yield a considerably higher significance in polarization detection. Figure 8 shows the expected detection significance for brighter GRBs, with different polarization fractions and angles of incidence. Different colors stand for different off-axis angles and we see that the polarization sensitivity of the CZTI is the highest at off-axis angles close to 45°, due to the higher effective area of the instrument at these

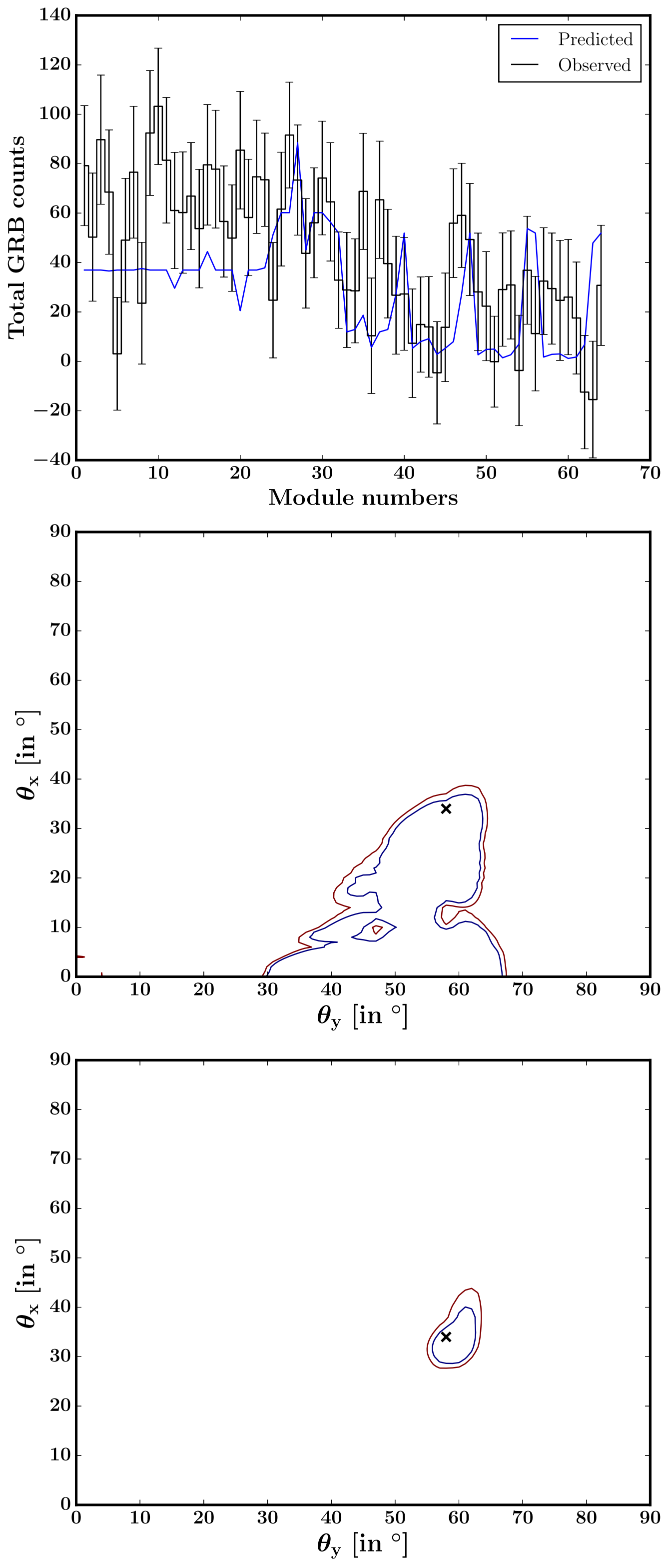

Figure 5. Top: the observed distribution of counts for the *Swift* position (see Figure 4) in the 64 CZT Modules of *AstroSat* CZTI instrument for GRB 151006A (histogram with errors). Each of the modules is blocked by the instrument materials in a different way and this is simulated by a ray-tracing model and shown as a histogram. Middle: contour plot of the χ^2 distribution of the observed and predicted counts for predictions based on various incident angles in local coordinates. The position of GRB 151006A is marked with a cross. The blue and brown χ^2 contours correspond to 90% and 99% confidence levels, respectively. Bottom: the χ^2 contours for a simulated burst with 1σ errors added by hand. Comparison with the contour obtained from the data indicates the presence of uncharacterized systematic errors in the data.

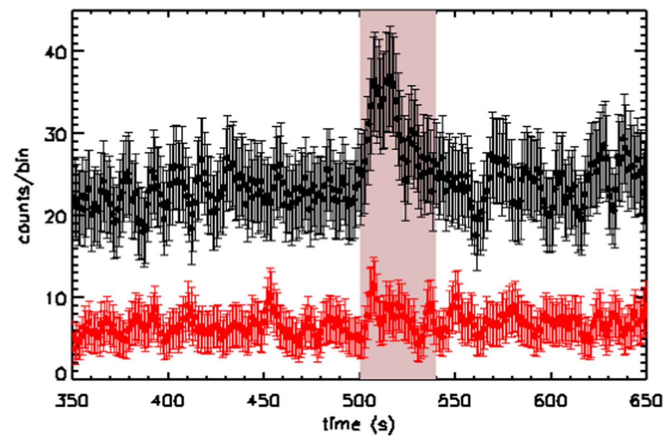

Figure 6. Observed rate of double events in CZTI during GRB 151006A. The events satisfying the Compton criteria (see the text) are shown in black and the red data points are those events not satisfying the Compton criteria. The shaded region in the light curve shows the prompt phase emission of GRB 151006A. The Compton events in this region are used for further analysis.

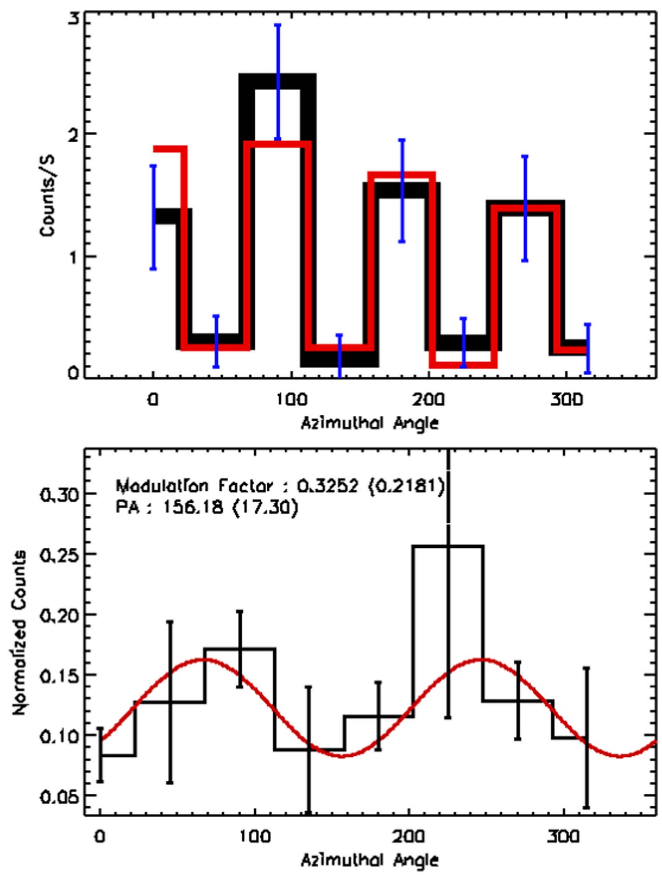

Figure 7. Top: background subtracted raw eight bin azimuthal angle distribution obtained from the Compton events are shown in black. The error bars shown in blue are the Poisson error on each azimuthal bin for a 68% confidence level. Azimuthal distribution shown in red is the one obtained by simulating with unpolarized radiation from the same GRB. Bottom: the geometrically corrected modulation curve for GRB 151006A. The red solid line is the $\cos^2\phi$ fit to the modulation curve. The fitted modulation factor is ~0.32 with a detection significance of 1.5σ. The fitted polarization angle is ~156° in the CZTI plane. Estimated errors (for 68% confidence level) on each parameter are given inside the bracket in the text.

angles. The solid and the dashed lines are obtained for polarization fractions of 0.5 and 0.7 respectively. For GRBs with fluence three or more times that of GRB151006A,

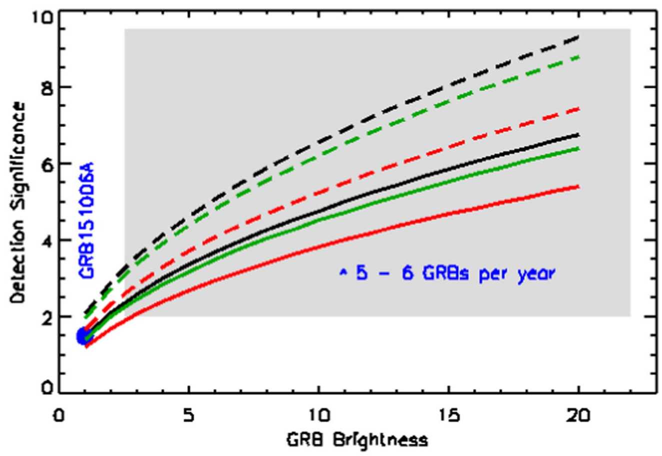

Figure 8. Expected polarization detection significance for GRBs with brightness (fluence) in the units of the brightness level of GRB151006A assuming spectra similar to that of GRB151006A and different polarization fractions (solid lines: 50% polarization, dashed lines: 70% polarization) and off-axis angles of detection (black: 40°, green: 60°, red: 20°). The filled green circle stands for the detection of GRB 151006A.

polarization may be estimated with a significance of more than 2.5σ. The CZTI is expected to detect polarization of five to six such GRBs per year. Statistical analysis of all these polarization measurements from CZTI along with other upcoming GRB polarimeters will be extremely useful in constraining the existing models of GRB prompt emission mechanism (Toma 2008).

4. DISCUSSION AND CONCLUSIONS

The CZTI detection of GRB 151006A, far off-axis, on the very first day of operation demonstrates the capabilities of CZTI as a wide-angle GRB monitor. Because the instrument had just been switched on, some of the parameters of the instruments were not finalized and tuned. For example, the low energy threshold was quite high (close to 30 keV instead of the design goal of 10–15 keV). Also, the Veto detector was not operating in anti-coincidence mode because the relevant timing parameters were not yet set. Nevertheless, observations of GRB 151006A have demonstrated several useful features of the instrument and the CZT Imager promises to be a good all sky monitor above 100 keV for transient events. The total effective area of CZT Imager (Figure 1) is comparable to that of *Fermi*. The fact that most of the satellite materials are transparent to X-rays above 100 keV makes the field of view of CZT Imager close to 3π steradians at these energies. Utilization of the observed data, however, requires a good description of the transparency of the satellite material and currently we are working on a complete satellite mass model to firm up the estimate of full-sky effective area as a function of viewing angle and photon energy.

Since the CZT Imager has a large area (~980 cm^2) detector with good position accuracy, the material distribution of the instrument and the satellite itself can be used as a coder to infer the incident direction of the transient events. Preliminary studies for this GRB have demonstrated that it should be possible to localize GRBs correct to a few degrees. A detailed investigation of several GRBs is being undertaken to better quantify the localization accuracy.

The most exciting feature of this new instrument is its capability to measure the polarization signals above 100 keV (Chattopadhyay et al. 2014; Vadawale et al. 2015). One good feature of the CZT Imager is the continuous availability of the time-tagged data so that no additional modes are required to be activated to measure the polarization signature. As mentioned earlier, this is the first time that hints of a polarization signal are reported for a GRB of fluence less than 2×10^{-5} ergs cm^{-2} and hence for bright GRBs the CZT Imager will provide polarization information with a vastly superior significance. Accurate estimate of the degree of polarization, measurement of time evolution of polarization properties and their relation to the spectral evolution have the potential to clearly distinguish between the various suggested models of GRB prompt emission mechanism. With its good spectral sensitivity, and capability to detect hard X-ray polarization, the CZT Imager promises to make a significant contribution to this investigation.

As an all-sky hard X-ray monitor, CZTI has sensitivity comparable to *Fermi* GBM and hence has the ability to detect possible hard X-ray transients associated with gravitational wave events (Connaughton et al. 2016; The LIGO Scientific Collaboration et al. 2016).

In summary, the CZT Imager on board *AstroSat* is a new addition to the suite of GRB instruments with an exciting new combination of capabilites such as spectroscopy, polarimetry, and localization. A detailed analysis of data from several GRBs is currently under way to fully characterize and refine these various features.

This publication uses data from the AstroSat mission of the Indian Space Research Organisation (ISRO), archived at the Indian Space Science Data Centre (ISSDC). CZT-Imager is built by a consortium of Institutes across India including Tata Institute of Fundamental Research, Mumbai, Vikram Sarabhai Space Centre, Thiruvananthapuram, ISRO Satellite Centre, Bengaluru, Inter University Centre for Astronomy and Astrophysics, Pune, Physical Research Laboratory, Ahmedabad, Space Application Centre, Ahmedabad: contributions from the vast technical team from all these institutes are gratefully acknowledged. We are thankful for the helpful discussions with K. L. Page, E. Troja, and C. Markwardt for *Swifthelp* facility. This research has also made use of data obtained through the High Energy Astrophysics Science Archive Research Center Online Service, provided by the NASA/Goddard Space Flight Center. R.B. is a stipendiary of the START program of the Polish Science Foundation (2016) and supported by Polish NCN grants 2013/08/A/ST9/00795, 2012/04/M/ST9/00780, 2013/10/M/ST9/00729, and 2015/18/A/ST9/00746.

REFERENCES

Atwood, W. B., Abdo, A. A., Ackermann, M., et al. 2009, ApJ, 697, 1071
Axelsson, M., Baldini, L., Barbiellini, G., et al. 2012, ApJL, 757, L31
Band, D., Matteson, J., Ford, L., et al. 1993, ApJ, 413, 281
Band, D. L. 2006, ApJ, 644, 378
Barthelmy, S. D., Barbier, L. M., Cummings, J. R., et al. 2005, SSRv, 120, 143
Basak, R., & Rao, A. R. 2015, ApJ, 812, 156
Bhalerao, V., Bhattacharya, D., Rao, A. R., & Vadawale, S. 2015, GRB Coordinates Network, Circular Service, No., 18422
Bhalerao, V., Bhattacharya, D., Vibhute, A., et al. 2016, arXiv:1608.03408
Burgess, J. M., Preece, R. D., Connaughton, V., et al. 2014, ApJ, 784, 17
Chattopadhyay, T., Vadawale, S. V., Rao, A. R., et al. 2016, Proc. SPIE, 9905, 99054D
Chattopadhyay, T., Vadawale, S. V., Rao, A. R., Sreekumar, S., & Bhattacharya, D. 2014, ExA, 37, 555
Coburn, W., & Boggs, S. E. 2003, Natur, 423, 415
Connaughton, V., Burns, E., Goldstein, A., et al. 2016, arXiv:1602.03920
Covino, S., & Gotz, D. 2016, arXiv:1605.03588

Dado, S., Dar, A., & De Rujula, A. 2007, arXiv:astro-ph/0701294
Gehrels, N. 2004, in AIP Conf. Ser. 727, Gamma-Ray Bursts: 30 Years of Discovery, ed. E. Fenimore & M. Galassi (Melville, NY: AIP), 637
Gehrels, N., & Mészáros, P. 2012, Sci, 337, 932
Gehrels, N., Ramirez-Ruiz, E., & Fox, D. B. 2009, ARA&A, 47, 567
Goldstein, A., Preece, R. D., Mallozzi, R. S., et al. 2013, ApJS, 208, 21
Götz, D., Covino, S., Fernández-Soto, A., Laurent, P., & Bošnjak, Ž. 2013, MNRAS, 431, 3550
Götz, D., Laurent, P., Lebrun, F., Daigne, F., & Bošnjak, Ž. 2009, ApJL, 695, L208
Gruber, D., Goldstein, A., Weller von Ahlefeld, V., et al. 2014, ApJS, 211, 12
Guiriec, S., Connaughton, V., Briggs, M. S., et al. 2011, ApJL, 727, L33
Iyyani, S., Ryde, F., Ahlgren, B., et al. 2015, MNRAS, 450, 1651
Kocevski, D., Barthelmy, S. D., Evans, P. A., Page, K. L., & Sbarufatti, B. 2015, GRB Coordinates Network, Circular Service, No., 18398
Lazzati, D., Rossi, E., Ghisellini, G., & Rees, M. J. 2004, MNRAS, 347, L1
McGlynn, S., Clark, D. J., Dean, A. J., et al. 2007, A&A, 466, 895
McGlynn, S., Foley, S., McBreen, B., et al. 2009, A&A, 499, 465
Medvedev, M. V. 2007, Ap&SS, 307, 245
Meegan, C., Lichti, G., Bhat, P. N., et al. 2009, ApJ, 702, 791
Meszaros, P., & Rees, M. J. 1993, ApJ, 405, 278
Nakar, E., Piran, T., & Waxman, E. 2003, JCAP, 10, 005
Norris, J. P., Bonnell, J. T., Kazanas, D., et al. 2005, ApJ, 627, 324
Page, K. L., Starling, R. L. C., Fitzpatrick, G., et al. 2011, MNRAS, 416, 2078
Pe'er, A., & Ryde, F. 2016, arXiv:1603.05058
Roberts, O. J., & Meegan, C. 2015, GRB Coordinates Network, Circular Service, No., 18404, 1
Ryde, F. 2005, ApJL, 625, L95
Ryde, F., & Pe'er, A. 2009, ApJ, 702, 1211
Singh, K. P., Tandon, S. N., Agrawal, P. C., et al. 2014, Proc. SPIE, 9144, 91441S
Sparre, M., & Starling, R. L. C. 2012, MNRAS, 427, 2965
The LIGO Scientific Collaboration, The Virgo Collaboration, Abbott, B. P., et al. 2016, arXiv:1602.03839
Toma, K. 2008, in AIP Conf Series Vol. 1040, Accelerators in the Universe: Interplay between High Energy Physics and Cosmology, ed. H. Kodama & K. Ioka (Melville, NY: AIP), 186
Vadawale, S. V., Chattopadhyay, T., Rao, A. R., et al. 2015, A&A, 578, A73
Vadawale, S. V., Rao, A. R., Bhattacharya, D., et al. 2016, Proc. SPIE, 9905, 99051F
Yonetoku, D., Murakami, T., Gunji, S., et al. 2011, ApJL, 743, L30
Yonetoku, D., Murakami, T., Gunji, S., et al. 2012, ApJL, 758, L1
Yoshida, A., Sakamoto, T., Takahashi, I., et al. 2015, GRB Coordinates Network, Circular Service, No., 18475